A high performance self-driven photodetector based on a graphene/InSe/MoS 2 vertical heterostructure

Zhesheng Chen, Zailan Zhang, Johan Biscaras, Abhay Shukla

To cite this version:

Zhesheng Chen, Zailan Zhang, Johan Biscaras, Abhay Shukla. A high performance self-driven photodetector based on a graphene/InSe/MoS 2 vertical heterostructure. Journal of Materials Chemistry C, 2018, 6 (45), pp.12407-12412. hal-01944295

HAL Id: hal-01944295

https://hal.sorbonne-universite.fr/hal-01944295v1

Submitted on 4 Dec 2018

HAL is a multi-disciplinary open access archive for the deposit and dissemination of scientific research documents, whether they are published or not. The documents may come from teaching and research institutions in France or abroad, or from public or private research centers.

L'archive ouverte pluridisciplinaire **HAL**, est destinée au dépôt et à la diffusion de documents scientifiques de niveau recherche, publiés ou non, émanant des établissements d'enseignement et de recherche français ou étrangers, des laboratoires publics ou privés.

High performance self-driven photodetector based on graphene/InSe/MoS_2 vertical heterostructure

Zhesheng Chen[1,2,3*], Zailan Zhang[4], Johan Biscaras[1], and Abhay Shukla[1*]

1 Institut de Minéralogie, de Physique des Matériaux et de Cosmochimie, Sorbonne Universités - UPMC Univ Paris 06, CNRS-UMR7590, 4 Place Jussieu, Paris 75252, France

2 Synchrotron SOLEIL, L'Orme des Merisiers, Saint-Aubin BP 48, Gif-sur-Yvette 91192, France

3 School of Nuclear Science and Technology, Lanzhou University, Lanzhou 730000, China

4 SZU-NUS Collaborative Center and International Collaborative Laboratory of 2D Materials for Optoelectronic Science & Technology, College of Optoelectronic Engineering, Shenzhen University, Shenzhen 518060, China

Corresponding Author:

*Email: zheshengchen@gmail.com and abhay.shukla@upmc.fr.

KEYWORDS: self-driven; built-in potential; graphene/InSe/MoS_2; heterostructure; photodetector

ABSTRACT: Hybrid Van Der Waals heterostructures comprising ultrathin layers of different materials and offering the possibility of novel properties and unusual charge transport characteristics have become a reality in recent years. Here, we vertically stack graphene, a transition metal dichalcogenide and a III-VI semiconductor together and report a novel self-driven photodetector based on graphene/InSe/MoS_2 heterostructure. The device shows rectifying and bipolar behavior. In the self-driven mode it exhibits high photoresponsivity (110 mA/W), fast photo-response (less than 1 ms) and high detectivity (over 10^{10} Jones). It also shows ambient operational stability over one month of operation and nearly uniform photocurrent distribution because of the efficient electron-hole pair separation arising from the large built-in potential at the interface of MoS_2 and InSe. Our graphene/InSe/MoS_2 heterostructure holds the promise for novel self-driven optoelectronics based on III-VI/ transition metal dichalcogenide heterojuctions.

TOC:

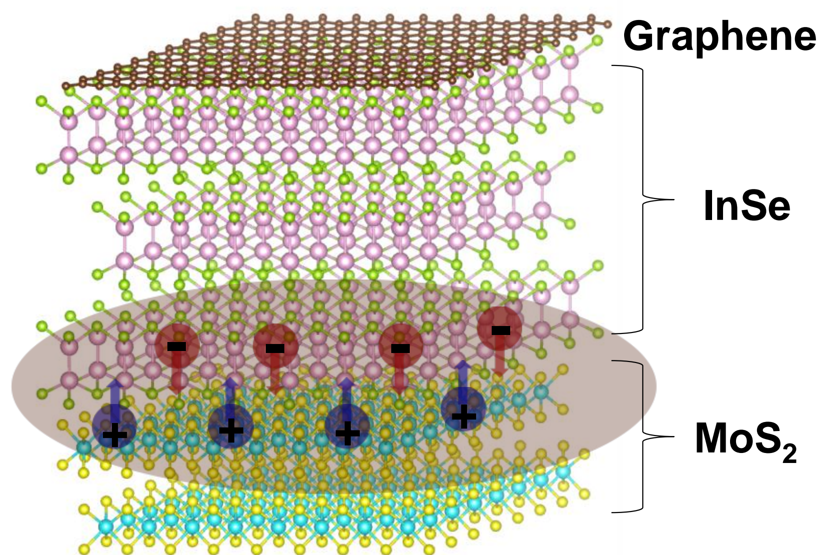

1. Introduction

Vertical Van Der Waals (VDW) heterostructures with different materials have attracted tremendous interest not only for their outstanding properties such as strong interlayer interaction and ultrafast charge transfer process but also in optoelectronic applications such as photodiodes, light emitting diodes (LED) and solar cells with self-driven and rectifying features [1-8]. The ultra-thin vertical VDW heterostructure is compatible with gating and the large junction area makes for an efficient and tunable device. The most studied vertical VDW heterostructures are p-n junctions assembled from various transition metal dichalcogenides (TMDs). For example, vertical MoS_2/WS_2 heterostructures show gate tunable diode like current rectifying behavior and can act as a photovoltaic cell or as a self-driven photodetector with photo-switching ratio exceeding 10^3. Moreover the collection of photo-excited carriers can be enhanced by adding top and bottom graphene layers [9]. In addition, other vertical VDW heterostructures with p-n junctions such as GaTe/InSe, black phosphorus/MoS_2 and SnSe/MoS_2 have been reported. All of them show diode-like behavior and photovoltaic effect due to the type-II VDW heterojunctions [10-13]. The self-driven behavior in a photodetector is based on the photovoltaic effect and should in principle be seen in devices based on type-II VDW heterojunctions because of the built-in potential. However the final performance is also determined by the properties of the hybrid device such as interlayer coupling, charge transfer and carrier lifetime. Few devices have been reported where the junction is between materials with the same kind of majority charge carriers like for example WS_2/MoS_2 with n-n type and Se/polyaniline with p-p type heterostructures[14,15],

in which similar rectifying properties and bipolar behavior can also exist. In our previous study, we combined n-type InSe with n-type MoS_2 and studied light interaction within vertical VDW InSe/MoS_2 heterostructures[16]. We found significant Raman intensity modification due to strong light coupling in the heterostrucure with a high quality interface and optimized light harvesting by controlling the layer thicknesses. In this work we add a monolayer graphene layer on top and fabricate a vertical graphene/InSe/MoS_2 heterostructure procuring three benefits: (1) ohmic contact between graphene and InSe; (2) efficient charge transport in graphene reducing carrier recombination[17]; (3) encapsulation of InSe by covering graphene layer thus enhancing the stability of the device[18]. Our graphene/InSe/MoS_2 device shows current rectifying and bipolar behavior and functions as an air-stable self-driven photodetector with nearly uniform photocurrent distribution, fast photo-response speed and high detectivity at zero bias and gate voltage.

2. Results and discussions

In the VDW graphene/InSe/MoS_2 heterostructure fabrication process, few-layer MoS_2 (~ 6 nm) was firstly mechanically exfoliated onto SiO_2/Si substrate and then multilayer InSe (~ 50 nm) was randomly dry transferred onto MoS_2, forming InSe/MoS_2 heterostructures. The interface between InSe and MoS_2 is very clean thanks to the dry transfer process and has been confirmed by our previous study[16]. Graphene was prepared on glass using the anodic bonding method[19] and wedging transferred onto the InSe/MoS_2 followed by plasma etching to complete

the graphene/InSe/MoS_2 heterostructure. The detailed fabrication process and corresponding optical images can be seen in supplementary information 1 and Figure S1.

The schematic diagram and optical image of graphene/InSe/MoS_2 heterostructure are shown in Figure 1 (a) and (b). The thickness of InSe is around 50 nm so as to maximize light absorption and the bottom MoS_2 layer is only 6 nm so as to optimize electrostatic doping by the back gate. In Figure 1(c), we characterize the heterostructure using Raman spectroscopy and show that vibration modes corresponding to InSe and MoS_2 are found in the range of 100 cm^{-1}~500 cm^{-1}. Moreover, the significant modification of Raman intensity (~5 times less from both InSe and MoS_2) in our graphene/InSe/MoS_2 heterostructure indicates interference effects and a good interface quality. In order to investigate the electronic band alignment between InSe and MoS_2, we measured the valence band electronic structure by means of angle resolved photoemission spectroscopy (ARPES) around the Brillouin zone center (Γ point) using the He Iα resonance line as shown in Figure 1(d) and (e). From the ARPES spectra of cleaved MoS_2 and InSe, one can deduce that the surface chemical potential is at 1.10 eV (MoS_2) and 0.98 eV (InSe) above the valence band maximum (Γ point) indicating intrinsic n-doping of these two semiconductors with band gaps of 1.33 eV (6 nm MoS_2) and 1.26 eV (bulk InSe) respectively. The high n-doping property in this two materials is consistent with earlier transport measurements (I_{ds}-V_{gs}) [20,21]. The electron affinity of InSe (-4.9 eV)[22] is smaller than that of MoS_2 (-4.3 eV)[23] causing ~0.7 eV difference of Fermi levels between the two materials before band alignment. However, when InSe and MoS_2 are in contact, the Fermi levels must coincide at the interface and a large built-in

potential is formed. The corresponding type II band alignment diagram of the InSe/MoS_2 heterostructure in Figure 1(f) shows that under illumination photoelectrons flow from InSe to MoS_2 thus causing a "self-driven" photocurrent without any applied bias or gate voltage.

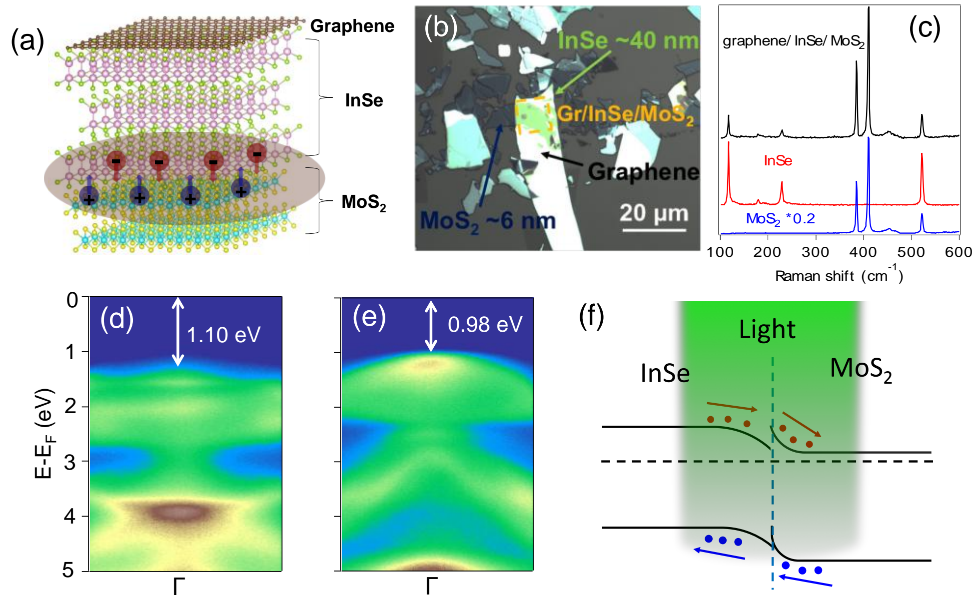

Figure 1. (a) Vertical VDW stacking, (b) the corresponding optical image and (c) Raman spectra of graphene/InSe/MoS_2 heterostructure. (d-e) ARPES spectra of MoS_2 and InSe acquired with He Iα resonance line. (f) Band alignment between InSe and MoS_2 at interface.

The schematic photodetector based on graphene/InSe/MoS_2 heterostructure is shown in Figure 2(a). It is worth pointing out that a Schottky barrier is known to exist at Au contacts on InSe [22,24]. An immediate benefit of the graphene layer on the top of the InSe/MoS_2 heterostructure is the ohmic contact between graphene and InSe[25]. The voltage between the source and drain determines the device current, and the voltage between the source and the back gate changes the Fermi level of the MoS_2 layer by electrostatic doping, which further modifies the band bending and the built-in potential at the interface. We first characterize the graphene/InSe/MoS_2 device by photocurrent mapping with 532 nm focused laser illumination without bias voltage or back

gate voltage as shown in Figure 2(b-c). The photocurrent is negative because photoelectrons flow from InSe (drain) to MoS_2 (source) under the influence of the built-in potential. It is uniformly -25 nA in the whole device (device area: ~180 μm^2) except the area surrounding the Au contact where it is higher. This is in contrast to the InSe/MoS_2 heterostructure without the graphene transport layer where the photocurrent vanishes rapidly away from the Au contact under the same illumination conditions, as shown in Figure S2. The non-uniform photocurrent distribution in the InSe/MoS_2 heterostructure and the nearly uniform distribution of the photocurrent in the graphene/InSe/MoS_2 heterostructure can be understood from the simplified device model shown in Figure 2 (d-e). In general, the total resistance of each device can be split up into several contributions and we will discuss them separately in the following. In a device based on the InSe/MoS_2 heterostructure as show in Figure 2 (d), the total resistance includes the contact resistance Au/InSe (R_1) and MoS_2/Au (R_8), the InSe ($R_{2,3,4}$) and MoS_2 ($R_{5,6,7}$) sheet resistance and the resistance at the InSe/MoS_2 interface R_D (we use a diode symbol here because of the rectifying behavior shown in Figure S3). However, InSe sheet resistance is several orders of magnitude higher than MoS_2 sheet resistance. During photocurrent mapping, the transport paths of photo-excited carriers differ depending on the spot where light is focused resulting in different measured device resistance. When light is focused close to the top Au contact, holes can move through InSe to the top Au contact easily because of the short distance, while electrons can also travel through MoS_2 to the other Au contact easily because of the low resistance. Thus the total resistance for current through the device can be schematized by $R_1 + R_D + R_5 + R_6 + R_7 + R_8$. When

light is focused away from the Au contact, total resistance for the current through the device is much higher due to the difficult hole transport through InSe schematized by R_1+ R_2+ R_3 +R_4 +R_D+ R_8. Thus the photocurrent decreases rapidly away from the top Au/MoS_2 contact. In contrast in the device based on graphene/InSe/MoS_2 heterostructure shown in Figure 2 (e), the sheet resistance of InSe is inconsequential because the graphene sheet short-circuits the InSe layer. In this case, photo-excited carriers travel through the InSe layer vertically and then laterally through the graphene layer because of the much higher mobility of graphene reducing carrier recombination and leading to a persisting photocurrent away from the Au contact. This is the second advantage of placing graphene on top of the InSe/MoS_2 heterostructure. The photocurrent is still not totally uniform in the whole graphene/InSe/MoS_2 device, with a somewhat higher current in the region close to the Au/MoS_2 contact because of the difference in the sheet resistance of graphene and MoS_2. This however could be corrected by fabricating a symmetric graphene/InSe/MoS_2/graphene heterostructure.

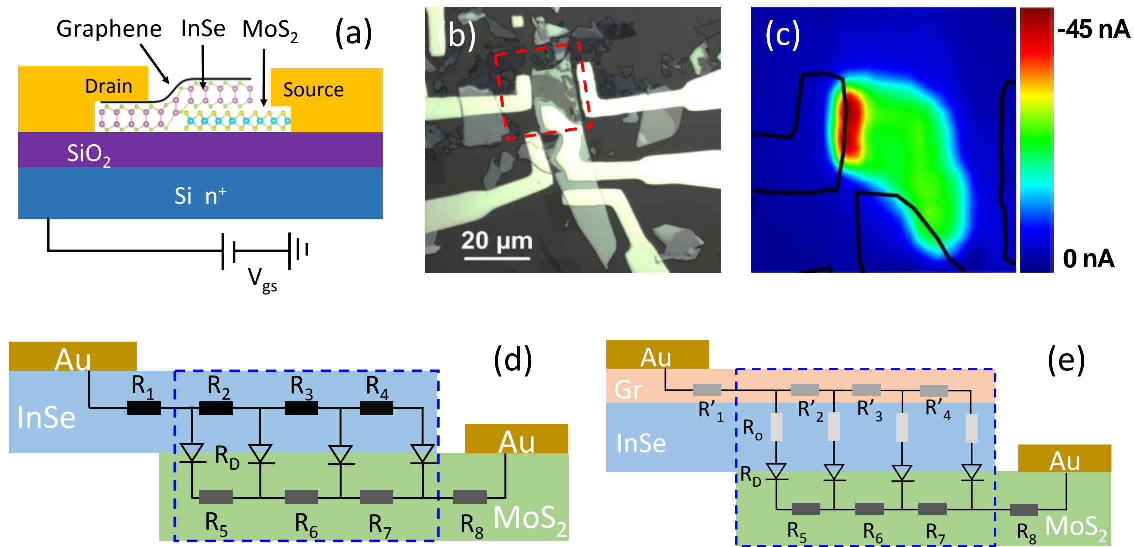

Figure 2. (a) Schematic of graphene/InSe/MoS_2 photodetector. (b-c) Nearly uniform photocurrent distribution in graphene/InSe MoS_2 heterostructure. The red dash square represents the corresponding photocurrent mapping area. (d-e) Schematics of the simplified device models based on InSe/MoS_2 and graphene/InSe/MoS_2 heterostructures.

We then measure drain-source current-voltage (I_{ds}-V_{ds}) curves in the absence of back gate voltage (V_{gs}=0 V) under different light illumination power as shown in Figure 3(a). The dark response shows diode-like behavior as seen from the insert of Figure 3(a), and under illumination the curves present the rectifying characteristics of a photodiode. The absolute photocurrent increases rapidly when the bias voltage assumes negative values and starts to saturate at a certain point depending on the illumination power. The photovoltaic effect is also observed in our device corresponding to a short-circuit current (I_{sc}) at zero V_{ds} or an open-circuit voltage (V_{oc}) at zero I_{ds} under illumination (Insert panel of Figure 2(a) and Figure S3). In the graphene/InSe/MoS_2 device, I_{sc} and V_{oc} are both higher than the values in the InSe/MoS_2 heterostructure at the same illumination power. For example, I_{sc} and V_{oc} are -4.8 nA and 220 mV

in graphene/InSe/MoS_2 device, three times higher than in the device without graphene (-1.5 nA and 70 mV) at the illumination power of 126 mW/cm^2, as shown in Figure S3. The photovoltaic effect leads to a self-driven device (V_{ds}=0 and V_{gs}=0). Figure 3 (b) shows the photo-response of the graphene/InSe/MoS_2 device in the self-driven mode and 532 nm incident light with 1.26 mW/cm^2 illumination power. Our device shows fast photo-response (τ) with both rise time and fall time less than 1 ms, which is three orders of magnitude less than that in homostructural InSe and MoS_2 photodetectors [26,27]. Furthermore we note that non-zero V_g can change the Fermi level in MoS_2, increasing (V_g>0) or decreasing (V_g<0) the Schottky interface barrier between InSe and MoS_2 and thus effectively modifying the photocurrent, as shown in Figure 3 (c). Finally, detectivity (D*) is another key parameter that represents the ability of the photodetector to distinguish signal from noise: $D^* = \frac{R\sqrt{A}}{\sqrt{2eI_{dark}}}$, where R is the photoresponsivity shown in Figure 4, A is the device area and I_{dark} is the dark current. In the self-driven mode, the D* in our graphene/InSe/MoS_2 heterostructure is as high as 1.08×10^{10} Jones (cm Hz$^{1/2}$/W) because of the high light on-off ratio caused by the large built-in potential between InSe and MoS_2.

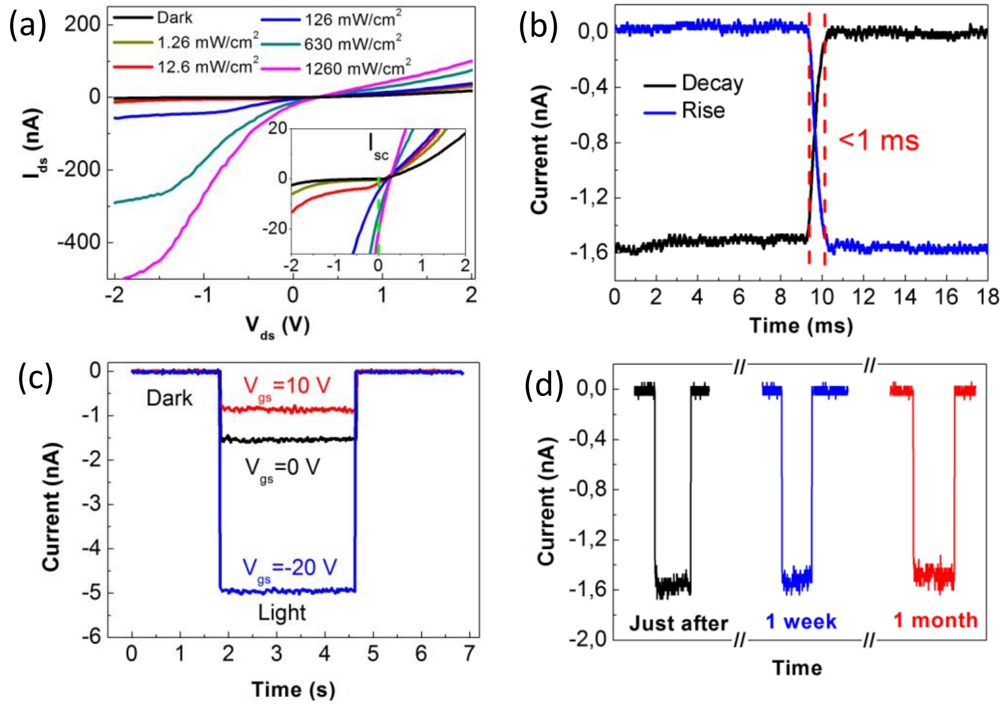

Figure 3. (a) I_{ds}-V_{ds} characterization of graphene/InSe/MoS_2 heterostructure as a function of illumination power. Insert: focused dark current and I_{sc}. (b) Rise (fall) time when light is turned on (off) from dark (illumination) status. (c) Photocurrent variation according to different back gate voltages. (d) Stability of graphene/InSe MoS_2 photodetector under ambient conditions and illumination power of 1.26 mW/cm^2.

The ambient stability of the device is an important criterion in applications of 2D materials. The stability of our graphene encapsulated device was characterized by monitoring the photocurrent and photo-response as a function of time as shown in Figure 3 (d). No change was observed over a month-long period under ambient conditions in strong contrast to the instability of a similar InSe/MoS_2 device (50% decrease in photocurrent over the same period as shown in Figure S4). The difference indicates that graphene plays a key role on the protection of InSe, which is in good agreement with Raman characterization from our previous study[18]. This is the third benefit of placing graphene on top of the InSe/MoS_2 heterostructure.

Figure 4 shows photoresponsivity ($R = I_{ph}/(P \times A)$, where I_{ph} is photocurrent and P is illumination power) and external quantum efficiency ($EQE = hcR/e\lambda$) of the graphene/InSe/MoS_2 photodetector calculated as a function of P from experimental data and fitted by the phenomenological function which has been used in non self-driven photodetectors: $R = \alpha P^{\beta-1}/A$, where α and β are fitting parameters[18,28]. Under 1.26 mW/cm^2 illumination power of 532 nm light, R and EQE are calculated to be 110 mA/W and 25.7 % in the self-driven mode. Both R and EQE decrease as P increases and moreover, this variation follows the power law very well with the fitting exponents $\alpha \approx 0.26$ and $\beta \approx 0.68$. This demonstrates that this fitting function can also be applied in self-driven photodetectors. We also compare these values with the performance R and EQE of InSe/MoS_2 photodetectors with different areas in Figure (4). In these devices, as mentioned earlier, the active area is only around the contacts so that R and EQE, which are normalized to area, decrease as the InSe/MoS_2 device area increase. However in the graphene/InSe/MoS_2 device, the whole detector area is active with a non-zero photocurrent as shown in Figure 2(c), which results in a much higher R and EQE compared to similar sized InSe/MoS_2 photodetectors. As explained earlier this is due to efficient transport of photo-excited carriers through monolayer graphene and significant reduction of electron-hole pair recombination during carrier transport.

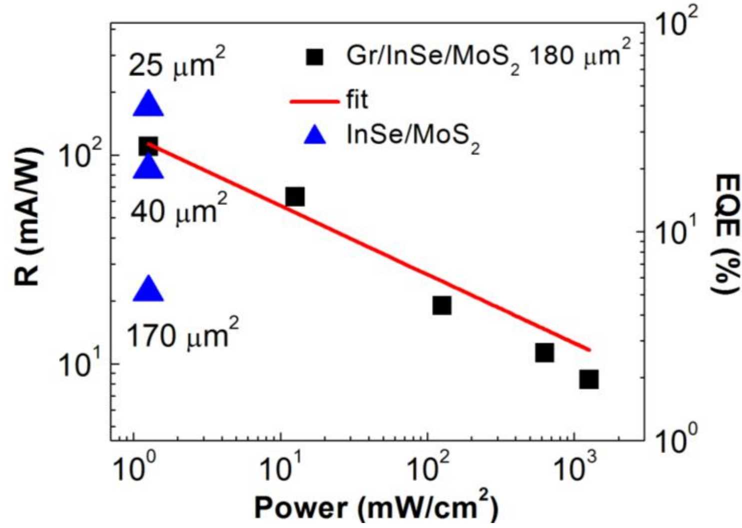

Figure 4. R and EQE as a function of illumination power for graphene/InSe/MoS_2 heterostructure and compared with different sized devices of InSe/MoS_2 heterostructures. Symbols: experiment data, red line: parameterized fit of phenomenological function (see text).

Table 1 summarizes the key parameters of our graphene/InSe/MoS_2 photodetector, and compares them to some InSe based and MoS_2 based vertical VDW heterostructure photodetectors in the self-driven mode published in literature. The R and τ in our graphene/InSe/MoS_2 device are comparable to that of the previously reported state-of-the-art devices. The detectivity in the device is two orders of magnitude higher than that of the $MoTe_2$/MoS_2 device. Again, we ascribe this to the large built-in potential at the InSe/MoS_2 interface and the high carrier mobility in the graphene layer.

Table 1. Comparison of key parameters between this work and some InSe based and MoS_2 based vertical VDW heterostructure photodetectors under self-driven mode. Only one other work calculated the detectivity explicitly.

Devices	thickness (nm)	R (mA/W)	D* (Jones)	τ(ms)	light intensity (mW/cm^2)	Ref
GaTe/MoS_2	4.5/3.5	1370	−	10	100	[29]
$MoTe_2$/MoS_2	3.3/7	46	1.06×10^8	0.06	~73	[30]
GaTe/InSe	18/10	13.8	−	0.02	0.16	[10]
MoS_2/perovskite	0.8/−	60	−	>200	0.7	[31]
Graphene/InSe/MoS_2	0.34/40/6	110	1.08×10^{10}	<1	1.26	This work

4. Conclusions

In summary, we fabricate a graphene/InSe/MoS_2 VDW heterostructure photodetector by random dry transfer of multilayer InSe on few-layer MoS_2 and wedging transfer of monolayer graphene on top. ARPES measurements show that both InSe and MoS_2 are highly n-doped and a type-II heterostructure is formed. In the self-driven mode, R and EQE are calculated at 110 mA/W and 25.65% which are comparable to other InSe based or MoS_2 based heterostructures. Compared to the InSe/MoS_2 device, the graphene/InSe/MoS_2 photodetector is active over the whole detector area with a nearly uniform photocurrent distribution and high operational stability under ambient conditions. It also has a high photoresponsivity of 110 mA/W, a fast photo-response time less than 1 ms and high detectivity resulting from a large built-in potential at the InSe/MoS_2 interface. The performance of our device indicates the promise of graphene encapsulated VDW heterostructures with III-VI and TMD semiconductors and highlights the benefits of a new generation of self-driven photodetectors.

Acknowledgement

This work was partly supported by French ANR project (Grant No. ANR-11-BS04-0019), by LABEX MATISSE through a post-doctoral grant, by "Investissement d'Avenir" Labex PLAM (ANR-10-LABX-0039-PALM) and a scholarship from China Scholarship Council (CSC, Grant No. 2011618135). We acknowledge the "Consortium des salles blanches d'Ile de France" for access to clean room facilities. We acknowledge M Rosticher and J Palomo for help with clean room work, and A. Chevy for the precursor materials used in this work.

Supporting Information

Fabrication process of graphene/InSe/MoS_2 heterostructure; photocurrent distribution in InSe/MoS_2 heterostructure; I_{ds}-V_{ds} measurement in InSe/MoS_2 photodetector and stability of InSe/MoS_2 photodetector under ambient condition.

References

1 H. Fang, C. Battaglia, C. Carraro, S. Nemsak, B. Ozdol, J. S. Kang, H. A. Bechtel, S. B. Desai, F. Kronast, A. A. Unal, G. Conti, C. Conlon, G. K. Palsson, M. C. Martin, A. M. Minor, C. S. Fadley, E. Yablonovitch, R. Maboudian and A. Javey, *Proc Natl Acad Sci USA*, 2014, **111**, 6198–6202.

2 F. Barati, M. Grossnickle, S. Su, R. K. Lake, V. Aji and N. M. Gabor, *Nature Nanotechnology*, 2017, 1–7.

3 X. Zhou, X. Hu, S. Zhou, H. Song, Q. Zhang, L. Pi, L. Li, H. Li, J. Lü and T. Zhai, *Adv. Mater.*, 2018, **30**, 1703286–8.

4 T. Yang, B. Zheng, Z. Wang, T. Xu, C. Pan, J. Zou, X. Zhang, Z. Qi, H. Liu, Y. Feng, W. Hu, F. Miao, L. Sun, X. Duan and A. Pan, *Nature Communications*, 2017, 1–9.

5 L. Ye, P. Wang, W. J. Luo, F. Gong, L. Liao, T. Liu, L. Tong, J. Zang, J. Xu and W. Hu, *Nano Energy*, 2017, 1–25.

6 X. Wang and F. Xia, *Nature Mater*, 2015, **14**, 264–265.

7 Y. Liu, N. O. Weiss, X. Duan, H.-C. Cheng, Y. Huang and X. Duan, *Nat. Rev.*

Mater., 2016, **1**, 16042–18.
8 M.-Y. Li, C.-H. Chen, Y. Shi and L.-J. Li, *Materials Today*, 2016, **19**, 322–335.
9 C.-H. Lee, *Nature Nanotechnology*, 2014, **9**, 676–681.
10 W. Feng, Z. Jin, J. Yuan, J. Zhang, S. Jia, L. Dong, J. Yoon, L. Zhou, R. Vajtai, J. M. Tour, P. M. Ajayan, P. Hu and J. Lou, *2D Mater.*, 2018, **5**, 025008–15.
11 Y. Deng, Z. Luo, N. J. Conrad, H. Liu, Y. Gong, S. Najmaei, P. M. Ajayan, J. Lou, X. Xu and P. D. Ye, *ACS Nano*, 2014, **8**, 8292–8299.
12 S. Yang, M. Wu, B. Wang, L.-D. Zhao, L. Huang, C. Jiang and S.-H. Wei, *ACS Appl. Mater. Interfaces*, 2017, **9**, 42149–42155.
13 J. Wong, D. Jariwala, G. Tagliabue, K. Tat, A. R. Davoyan, M. C. Sherrott and H. A. Atwater, *ACS Nano*, 2017, **11**, 7230–7240.
14 N. Huo, J. Kang, Z. Wei, S.-S. Li, J. Li and S.-H. Wei, *Adv. Funct. Mater.*, 2014, **24**, 7025–7031.
15 P. Yu, K. Hu, H. Chen, L. Zheng and X. Fang, *Adv. Funct. Mater.*, 2017, **27**, 1703166–10.
16 Z. Chen, J. Biscaras and A. Shukla, *2D Mater.*, 2017, 1–8.
17 W. Luo, Y. Cao, P. Hu, K. Cai, Q. Feng, F. Yan, T. Yan, X. Zhang and K. Wang, *Advanced Optical Materials*, 2015, **3**, 1418–1423.
18 Z. Chen, J. Biscaras and A. Shukla, *Nanoscale*, 2015, **7**, 5981–5986.
19 K. Gacem, M. Boukhicha, Z. Chen and A. Shukla, *Nanotechnology*, 2012, **23**, 505709–6.
20 W. Feng, W. Zheng, W. Cao and P. Hu, *Adv. Mater.*, 2014, **26**, 6587–6593.
21 S. Das, H.-Y. Chen, A. V. Penumatcha and J. Appenzeller, *Nano Lett.*, 2012, **13**, 100–105.
22 X. Zaoui, R. Mamy and A. Chevy, *Surface Science*, 1988, **204**, 174–182.
23 M. Farmanbar and G. Brocks, *Phys. Rev. B*, 2015, **91**, 161304–5.
24 R. Mamy, X. Zaoui, J. Barrau and A. Chevy, *Revue de Physique Appliquée*, 1990, **25**, 947–950.
25 G. W. Mudd, S. A. Svatek, L. Hague, O. Makarovsky, Z. R. Kudrynskyi, C. J. Mellor, P. H. Beton, L. Eaves, K. S. Novoselov, Z. D. Kovalyuk, E. E. Vdovin, A. J. Marsden, N. R. Wilson and A. Patanè, *Adv. Mater.*, 2015, **27**, 3760–3766.
26 S. R. Tamalampudi, Y.-Y. Lu, R. Kumar U, R. Sankar, C.-D. Liao, K. Moorthy B, C.-H. Cheng, F.-C. Chou and Y.-T. Chen, *Nano Lett.*, 2014, **14**, 2800–2806.
27 Z. Yin, H. Li, H. Li, L. Jiang, Y. Shi, Y. Sun, G. Lu, Q. Zhang, X. Chen and H. Zhang, *ACS Nano*, 2011, **6**, 74–80.
28 Z. Sun, Z. Liu, J. Li, G.-A. Tai, S. P. Lau and F. Yan, *Adv. Mater.*, 2012, **24**, 5878–5883.
29 S. Yang, C. Wang, C. Ataca, Y. Li, H. Chen, H. Cai, A. Suslu, J. C. Grossman, C. Jiang, Q. Liu and S. Tongay, *ACS Appl. Mater. Interfaces*, 2016, **8**, 2533–2539.

30 Y. Chen, X. Wang, G. Wu, Z. Wang, H. Fang, T. Lin, S. Sun, H. Shen, W. Hu, J. Wang, J. Sun, X. Meng and J. Chu, *Small*, 2018, **14**, 1703293–7.

31 F. Bai, J. Qi, F. Li, Y. Fang, W. Han, H. Wu and Y. Zhang, *Adv. Mater. Interfaces*, 2018, **10**, 1701275–9.